Extreme Wave Front Sensing Accuracy for the Eclipse Coronagraphic Space Telescope

Joseph J. Green*, David Redding, Stuart Shaklan and Scott A. Basinger
Jet Propulsion Laboratory; 4800 Oak Grove Dr., Pasadena, CA 91109

ABSTRACT

The Eclipse coronagraphic telescope will allow for high contrast imaging near a target star to facilitate planet finding. One key element will be its high accuracy, high authority deformable mirror (DM) that controls the wave front error (WFE) down to an acceptable level. In fact, to achieve the desired contrast ratio of nine orders of magnitude (in intensity) to within 0.35 arcseconds of the target star, the WFE in the telescope must be controlled to level below 1Å rms within the controllable bandwidth of the DM. To achieve this extreme wave front sensing (WFS) accuracy, we employ a focus-diverse phase retrieval method extended from the Next Generation Space Telescope baseline approach. This method processes a collection defocused point-spread functions, measured at the occulting position in the Eclipse optical system, into a high accuracy estimate of the exit-pupil WFE. Through both simulation and hardware experiments, we examine and establish the key data requirements, such as the defocus levels and imaging signal-to noise level, that are necessary to obtain the desired WFS accuracy and bandwidth.

Keywords: Coronagraphic telescope, wave front sensing, wave front control, phase retrieval, focus-diversity

1. INTRODUCTION

The direct detection of extra-solar planets is a daunting task. The reflected light from an extra-solar Jovian planet is typically nine orders of intensity fainter than its parent star. Even in the absence of optical aberrations, the diffracted light from the limiting telescope aperture alone washes out any light arriving from the much fainter planet. To mitigate the effects of diffraction from the parent star, the Eclipse coronagraphic telescope employs a combination of an occulting spot and Lyot stop, [1]. In addition to the coronagraph, Eclipse will employ a high accuracy, high authority DM to control the wave front errors (WFE) presented by the optical system, [2].

The DM in the Eclipse telescope plays an essential role in the goal of planet finding. Optical aberrations in the system cause light to be scattered away from the occulting spot and can quickly deteriorate the achievable contrast level in the imagery. With a regular grid of actuators, a DM can create a "dark-hole" in the image plane about the optical axis as the controllable WFE is compensated, [3]. To achieve the nine orders of magnitude in intensity contrast at visible wavelengths, the WFE in Eclipse must be controlled to a level below 1 Angstrom rms. Of coarse controlling the wave front down to this level not only requires a high precision DM, but the capacity to sense the WFE at an extreme level of accuracy.

Recently, a method for correcting the WFE after the Eclipse coronagraph has been proposed, [4]. By operating after the coronagraph, this approach takes advantage of the tremendous reduction in diffracted light from the on-axis star. Using spatially filtered images of the Lyot plane, the uncontrolled WFE in the system can be efficiently sensed and controlled. It is unclear, however, how optical aberrations and scattering that occur after the Lyot plane may bias this approach. Instinctively, we expect that the best occultation comes about by correcting for only the optical aberration that occurs prior to the occulting spot. As such we consider a method for WFS that uses images taken about the occulting plane rather than after the coronagraph.

* Contact information: 4800 Oak Grove Dr., M/S 306-336, Pasadena CA 91109, E-mail: Joseph.J.Green@jpl.nasa.gov

Recently, the baseline image based phase retrieval algorithm under consideration for the Next Generation Space Telescope (NGST) has been experimentally validated to be accurate to levels below $\lambda/100$, [5]. The modified Gerchberg-Saxton algorithm (MGS) uses an image of the optical system pupil along with a diverse set of defocused point-spread function (PSF) measurements to estimate the phase across the exit pupil, [6]. NGST plans to use such an approach to achieve the initial alignments and for the regular maintenance of its optical telescope assembly.

In this paper we study the inner workings of MGS algorithm. After briefly reviewing the method, we examine its error sensitivity to photon and measurement noise as well as to many forms of modeling errors. From this analysis we show that with strict constraints on data requirements along with a proposed preprocessing algorithm, MGS can produce estimates of WFE in the optical system with accuracy levels that exceed $\lambda/10000$.

2. THE MODIFIED GERCHBERG SAXTON ALGORITHM

2.1 Amplitude Constraints In the Algorithm

Before we can discuss the MGS algorithm itself, we must first review the mathematics of defocused PSF image formation. The complex pupil function in the presence a particular level of defocus is given by

$$p_i(u;\lambda) = \begin{cases} a(u)\cdot \exp\left[j\frac{2\pi}{\lambda}\left(\theta(u) + 4\lambda d_i u^2\right)\right] & |u| \le \frac{1}{2} \\ 0 & \text{otherwise} \end{cases}, \tag{1}$$

where $a(u)$ is the exit-pupil amplitude function, $\theta(u)$ is the unknown optical path difference (OPD) function, λ is the optical wavelength and d_i is the defocus level in waves. In incoherent, monochromatic light, the far-field intensity pattern is proportional to the modulus-squared Fourier Transform of the exit pupil function, [7]. Over a finite optical passband this intensity pattern can be expressed as

$$g_i(x) \propto \int_{\lambda_{min}}^{\lambda_{max}} w(\lambda)\cdot \left| P_i\left(\frac{x}{\lambda F}\right)\right|^2 d\lambda. \tag{2}$$

The function $P_i(x/\lambda F)$ represents the Fourier transform of equation (1) which is scaled by the wavelength and F/# of the optical system. The function $w(\lambda)$ weights the monochromatic far-field patterns by the net optical passband produced by the light source and system throughput. MGS converts the defocused PSF intensity measurement into a far-field amplitude constraint during processing as follows

$$\left|\hat{P}_i(x)\right| = \left|\tilde{g}_i(x)\right|^{1/2}, \tag{3}$$

where $\tilde{g}_i(x)$ is a normalized version of $g_i(x)$. Similarly, the pupil intensity measurement is converted into to a pupil plane amplitude constraint as stated by

$$\left|\hat{p}(x)\right| = \left|\tilde{g}_{pupil}(x)\right|^{1/2}. \tag{4}$$

2.2 Iterative Procedure for Estimating Phase

As in the Gerchberg-Saxton phase retrieval algorithm, [8], the PSF image measurements are used to constrain the amplitude during processing. Rather than constraining just the pupil support, MGS also constrains the interior pupil amplitude function. As an additional innovation, the MGS allows for the inclusion of a large defocus term in the inner loop. While this makes the approach similar to the method proposed by Misell, [9], MGS iteratively processes an ensemble of defocused PSFs separately against the pupil amplitude constraint to obtain a set of estimates. Each phase estimate is then unwrapped (if necessary) and combined together to form the current joint estimate. This combined estimate is subsequently fed back as an initial starting point for the next round of processing.

The processing that occurs independently for each defocused PSF has two steps in each iteration. In the first step, the phase at the far-field (image-plane), $\hat{\phi}_i^n(x;\lambda_O)$, is computed from the complex exit-pupil estimated in the previous iteration,

$$\hat{\phi}_i^n(x;\lambda_o) = \angle\left(\mathcal{F}\left\{|\hat{p}_i(x)|\cdot\exp\left[j\frac{2\pi}{\lambda_o}\left(\hat{\theta}_i^{n-1}(x)+4\lambda_o d_i u^2\right)\right]\right\}\right) \tag{5}$$

In this equation, the complex far-field pattern is computed at nominal imaging wavelength λ_o. This pattern is computed using the measured pupil amplitude, equation (4), and the pupil-phase from the prior iteration. The phase of the complex far-field is thus retained as the current estimate for that domain.

In the second step of an inner iteration, the current estimate of the far-field phase is combined with the measured PSF amplitude, equation (3) and together they are propagated back to the pupil-plane. The known defocus aberrations is subsequently removed and remaining phase term becomes the current estimate of the exit-pupil OPD map, as stated by

$$\hat{\theta}_i^n(u;\lambda_o) = \left(\frac{\lambda_o}{2\pi}\right)\cdot\angle\left(\mathcal{F}^{-1}\left\{\left|\hat{P}_i(x)\right|\cdot\exp\left[j\hat{\phi}_i^n(x)\right]\right\}\times\exp\left[-j8\pi d_i u^2\right]\right). \tag{6}$$

As mentioned earlier, after a round of these "inner iterations" are conducted the independent OPD estimates are combined together

$$\hat{\theta}^N(u;\lambda_o) = \frac{1}{M}\sum_{i=1}^{M}\hat{\theta}_i^N(u;\lambda_o). \tag{7}$$

This combined result becomes this initial estimate for the next round of inner-iterations. In this paper, we examine the impact of stochastic and modeling error sources on the inner-loop performance. With an understanding of these error sensitivities, we develop data requirements and algorithm modifications that enable this approach to provide sub-angstrom levels of accuracy. Refer to [6] for a more complete discussion of the NGST MGS algorithm in its entirety.

3. SENSITIVITY TO STOCHASTIC ERROR SOURCES

The far-field intensity pattern that is predicted by equation (2) is only absolutely correct in the absence of noise. Because imaging is fundamental a photon-counting process, the intensity pattern that is built up over an integration time follows Poisson statistics [10]. Poisson noise is a signal-dependent noise source. As the integration time increases and more photons are counted, the effective SNR in the image increases as the square root of time.

To study the impact Poisson noise has on the MGS WFS accuracy, we conducted a set of Monte Carlo simulation. In each realization in the study, an instance of the OPD map was generated using point-wise independent, white Gaussian noise. Using an OPD map instance we generated defocused, monochromatic PSF that was then given to a Poisson noise generator to realize a quantum-limited image. Using a perfect zero-one function for the pupil amplitude, we conducted a single-frame MGS estimation of the OPD with which we computed error statistics.

We exercised this simulation over a large range of imaging scenarios where photon-counts, defocus levels and processing levels were varied. Figure 1 shows the characteristic behavior of the MGS as a function of the number of photons. The number of inner loop iterations, *N*, wave varied from 25 to 500. For a small level of processing the WFS performance hits a floor for larger levels of integrated flux. This apparent performance floor reduces as the number of iterations of MGS is increased. This is an indication the estimates were *under*-processed. Not surprisingly, this behavior is reversed at low light levels. Here, *over*-processing the data causes the algorithm the fit the noise in the images and ultimately reduce the fidelity of the estimates.

From the set of simulations we developed an empirical model for WFS error as function of the total number of photons collected, which is stated by,

$$\left(\frac{\sigma_{WFS}}{\lambda}\right)^2 = \alpha_{PN}\times\frac{N_{opd}}{N_{photons}}. \tag{8}$$

Here, $N_{photons}$, represents the number of photons collected in the defocused PSF measurements. The scalar, α_{PN}, has a nominal value of about 0.01 and is dependent upon the level of convergence achieved in the solution. N_{opd} represents the number of elements in the OPD map estimate. Because we use fast Fourier transforms (FFT) in these simulations and a circular pupil function, we can express N_{opd} as through the array size, N_{FFT}, as stated by

$$N_{OPD} = N_{FFT} \cdot \left(\frac{2}{q}\right)^2 \cdot \left(\frac{\pi}{4}\right), \tag{9}$$

where $q = \lambda F / \Delta$ with Δ representing the pixel size. It should be noted that when q equals two, the images are critically sampled, [11].

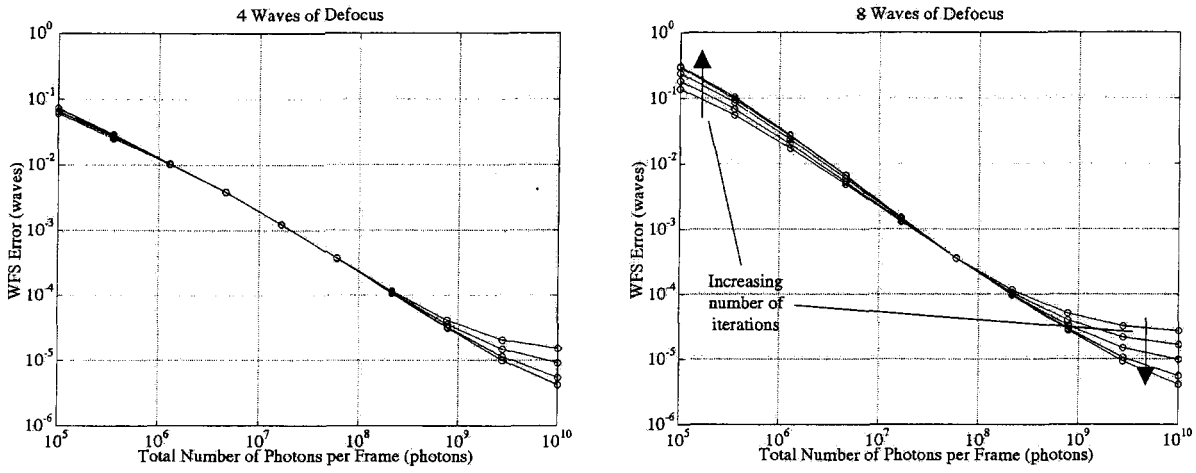

Figure 1: WFS error as a function of the total number of photons collected for 4 (left) and 8 (right) waves of defocus.

The empirical result shown in equations (8) appears to be in excellent agreement with the results of conducting WFS at the re-imaged Lyot plane (RLP), [4]. In the case of the RLP, the variance of the phase estimation error in radians goes as $1/\bar{n}$, where $\bar{n}$ is equal to the number of photons per coherent cell. Ignoring the circular support of the OPD, there is essentially equality between N_{opd} and $N_{photons}/\bar{n}$. The consistency between these WFS error expressions is a strong indication of an equivalence of the SNR for sensing at the occulting plane and at the RLP.

In addition to Poisson noise, read-noise is another stochastic source of WFS error. As can be seen in figure 1, the total integrated flux that is required to reach $\lambda/10000$ is on the order of 10^9 photons. It can be shown that the average number of photons per pixel goes as

$$\langle g_i(x) \rangle \propto \frac{N_{photons}}{\pi \cdot (8d_i)^2}, \tag{10}$$

over the support of the defocused PSF. Read noise is typically a small fraction of the full well capacity of the detector. In the case were we have 10^9 photons in a PSF with 8 waves of defocus, the average intensity is on the order $8\text{x}10^4$ photons. In science grade cameras for imaging at visible wavelength, typical read-noise levels range from 5-20 electrons rms. In term of noise variance, Poisson noise is clearly the dominant noise source when striving for extreme sensing accuracy.

4. FIXED MODEL MISMATCH ERRORS AND DEFOCUS SYMMETRY

MGS evolves estimates of the phase at the pupil and focal planes by successively propagating a complex optical field though the system model. Any mismatch in the assumed system model or non-optical effects appearing in the data results in errors propagating into the phase estimate. As we demonstrate in section, even small mismatches can be detrimental to the accuracy of a single defocus level-based OPD estimate.

Fortunately, when a modeling error is fixed by the algorithm assumptions, the resulting OPD errors are greatly reduced when the estimates are generated from a symmetrically defocused pair of PSFs. At the end of the inner-loop set of iterations, the WFS errors caused by the mismatch appear nearly identical on each side of focus but with opposite signs. When the individual estimates are subsequently combined in the outer loop, these errors largely cancel out. In this section, we explore several forms of fixed model mismatch. Through simulations, we demonstrate the level of WFS error reduction that was obtained by processing symmetrically defocused PSF measurements.

4.1 Imperfect Pupil Amplitude Knowledge

MGS uses both PSF and pupil intensity measurements as a basis for constraining the field amplitudes during processing. Errors in the amplitude and support of the assumed pupil function propagate into the OPD estimates. Figure 2 compares the WFS accuracy obtainable with a single defocused PSF to that using a pair of PSFs taken symmetrically about focus. The top set of curves represent the single PSF performance of MGS using 4, 6 and 8 waves of focus while the bottom curves represent performance from the symmetrically defocused pair. As can be seen in figure 2, the defocus symmetry provides a substantial three orders of magnitude of error cancellation. We suspect that the pupil amplitude contribution is canceling in the same sense that it cancels in curvature sensing, [12], where the local amplitude variations appears as curvatures of opposites sign on each side of focus.

4.2 Imaging with Broadband Light

Looking back at equations (5) and (6), we can see that MGS is fundamentally a monochromatic algorithm. Broadband light induces a continuous range of defocus levels and spatial scaling in to single defocused PSF measurement. As such, there is no singular choice for imaging wavelength nor OPD zero-padding that will avoid inducing a model mismatch. In Figure 3, we compare the performance of estimation using a single defocus level with the performance from a symmetric pair of defocus levels. Clearly, the single-frame WFS performance is nowhere near the accuracy level required for high-contrast imaging. Fortunately, the focus symmetry enables there to be a substantial error cancellation when the pair of independent inner MGS estimates are combined.

4.3 Incoherent Gaussian Blur

Any jitter and drift that occurs on the line of sight during integration will impose a level of blurring into the defocused PSF images. Additionally, the detection process itself will introduce a blurring effect due to inter-pixel leakage. Because this blurring occurs on the field intensity, we refer to this as an incoherent process. We studied the impact of incoherent blurring by convolving simulated defocused PSF measurements with a Gaussian function of various sizes. Figure 4 show the resulting WFS error from processing single and symmetric pairs of defocused PSFs.

As before we find that the focus symmetry greatly reduced the algorithm sensitivity to the blur induced modeling mismatch. Interestingly, the WFS error we observe is now dependent upon the level of WFE in the system itself. As the WFE in the system is reduced, the WFS error also diminishes. In figure 4, we show only the result for a $\lambda/10000$ rms WFE, where the benefits of symmetric defocus are the weakest. Even at this level, using symmetrically defocused PSFs largely mitigates the added error due to blur.

4.4 Imaging with Pixels

In addition to blurring, the detection process introduces a binning process. The incident light on the detector is integrated over the area of each pixel. Thus the samples in the image data are not intensity measurements at exact field locations but rather measurements integrated in binned regions about the field locations. To study the impact of binning, we generated over-sampled PSFs that were subsequently binned down to simulate the finite area of the pixels. In figure 5, we show that for a single defocus-level based estimate, the WFS error is on the order of $\lambda/500$ and is independent of the aberration level. Using a symmetrically defocused PSF pair, we again obtain a substantially improved performance that is now coupled to the level of WFE in the optical system.

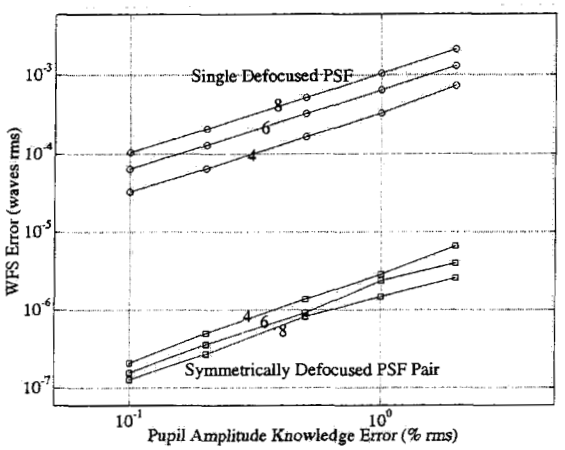

Figure 2: WFS error level induced by impefect pupil amplitude knowledge.

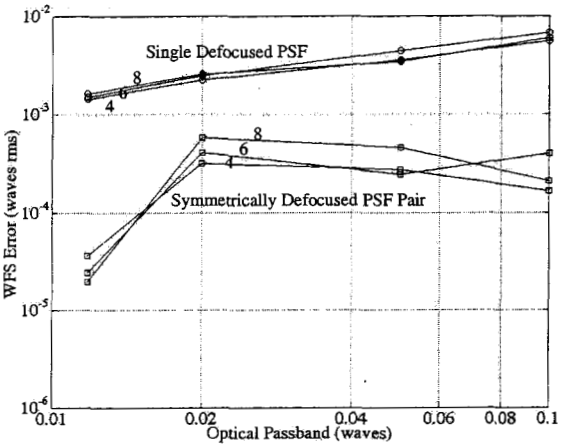

Figure 3: WFS error level induced by the optical bandwidth of the light.

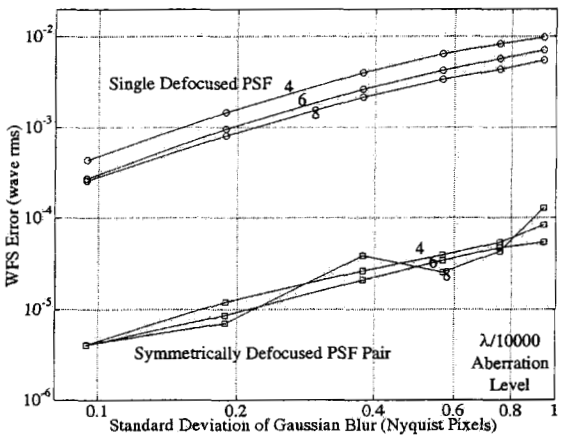

Figure 4: WFS error level induced by incoherent Gaussian blurring.

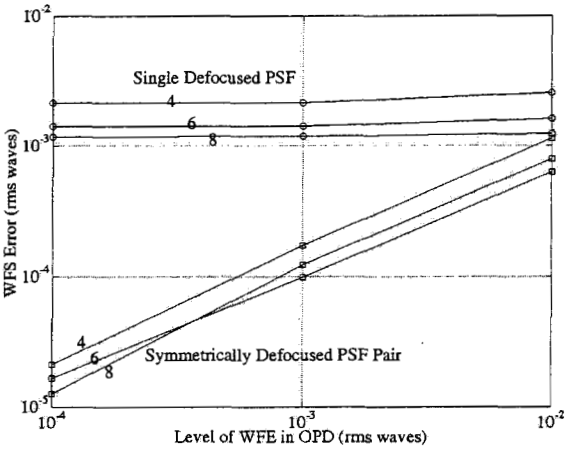

Figure 5: WFS error level induced by a binning process.

5. MITIGATING DYNAMIC MODEL MISMATCH ERRORS

While it is fortunate that the impact of fixed modeling errors is largely mitigated using pairs of PSFs taken symmetrically about focus, there exist sources of dynamic modeling errors. Dynamic modeling errors are mismatches between the model and the physical system that are not fixed by assumptions but are induced by dynamics in the imaging system. In this section we explore the two such error sources: PSF centering errors and defocus level modeling errors. For these error sources we look at the WFS error that is caused by the presence of centering and defocus model errors and show how to mitigate the impact with proper adaptation of the WFS algorithm model.

5.1 PSF Centering Errors

When PSF measurements are made, the actual location of the PSF is often different than the presumed optical axis in the WFS algorithm. In practice, the PSF measurement is centered to bring its alignment into consistency with the algorithm assumptions. Unfortunately, residual centering errors translate into WFS error. In addition to phase tilt, the mismatch between the true optical axis and the system model causes the MGS algorithm to develop false coma and other higher order errors in its estimate. In figure 6, we show how tilt and higher order WFS errors are introduced into an OPD estimate as a function of the PSF center offset and defocus level.

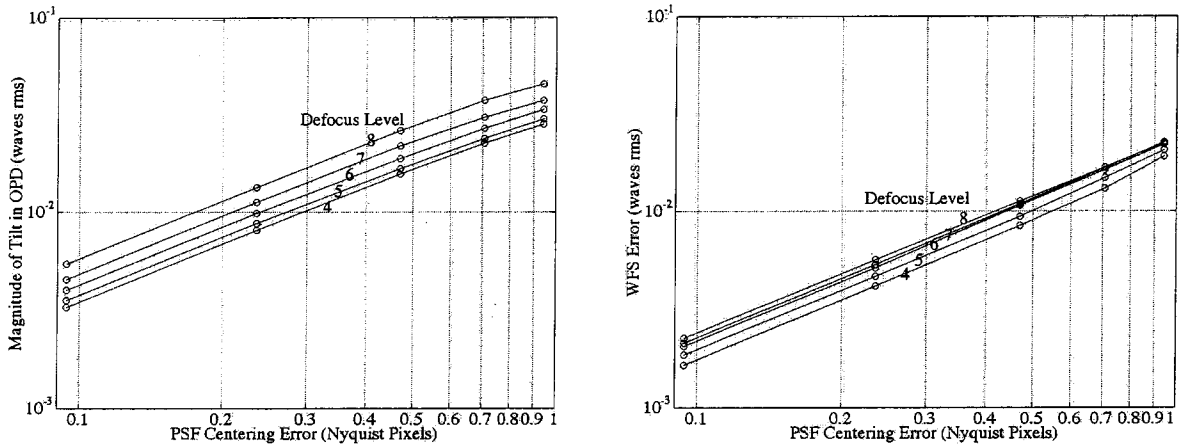

Figure 6: An error in the centering of a PSF measurement induces tilt (left) as well as errors in the resulting OPD estimate (right).

Although this is not shown here, we find that the WFS error will only cancel when processing symmetrically defocused PSFs that are perfectly co-registered with each other. In this particular case, the OPD estimate will contain only an additional tilt terms that is directly related to the common offset the PSF pair to presumed optical axis in the model. Because there is no guarantee that the centering errors will be identical from image to image, we cannot rely on the error cancellation from symmetric defocus. Fortunately the MGS algorithm itself offers a solution.

The tilt term that is recovered in a single frame OPD estimate is still proportional to the residual centering error. In fact we find that for a fixed level of processing the residual PSF centering error can be approximated by

$$\Delta_x = +\alpha_{tilt} \cdot z_2 \cdot d^{3/4}$$
$$\Delta_y = -\alpha_{tilt} \cdot z_3 \cdot d^{3/4}, \quad (11)$$

where z_2 and z_3 are respective Zernike coefficients for x and y tilt in waves, [13]. The constant, α_{tilt}, ranges between 5 and 7 depending on the amount of processing. Using equation (11) as an estimate of the residual offset, we can improve upon the PSF centering using sub-pixel shifts. The process of estimating the OPD and subsequent estimating the PSF center offset can be iterated to greatly improve upon the PSF centering and reduce the centering errors.

5.2 Defocus Model Error

The mechanisms used to provide focus diversity in the PSF measurements are not perfect. As with knowledge of the optical axis in a given PSF measurement, the level of defocus that is induced in a PSF is known to only a finite level of accuracy. In figure 7, we show that we get the expected defocus aberration in our estimates in proportion to the error in our defocus level assumptions. In addition to the defocus term, there are substantial higher order terms that are also introduced into the estimate which increase the WFS error level.

The disparity in the recovered defocus term with the defocus level in PSF is most likely due incomplete algorithm convergence given a fixed level of processing. As with the mitigation of centering error, we correct the error in the assumed level of defocus by adding in the focus term observed in an OPD estimate. With this updated prior model, we conduct another phase retrieval and observe the residual level of the defocus aberration in the estimate. This process is iterated until the defocus residual is at an acceptable level.

In figure 8, we present a schematic for a method of concurrently adapting the model and data to mitigate the defocus and centering mismatches. In this approach, we compute single frame estimates for each level of defocus to develop simultaneous refinements to the inherent modeling errors. This process is iterated until the residual OPD tilt and defocus terms are reduced to an acceptable level for all the defocus frames. After this processing is completed, the centered PSFs and refined defocus prior models are given to the MGS algorithm to compute the final estimate of the OPD.

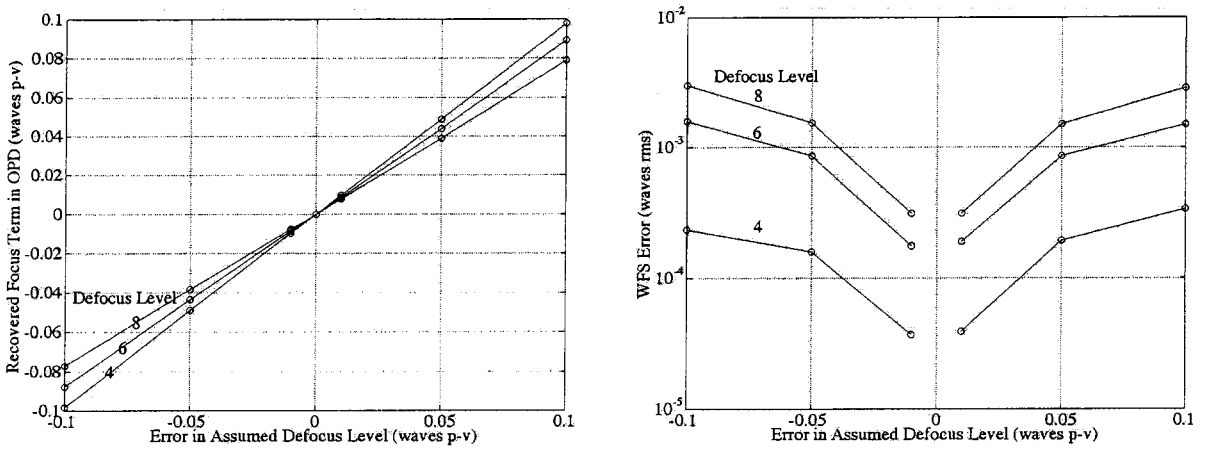

Figure 7: Errors in the defocus level model induce a focus term in the OPD (left) as well as high order WFS Error terms (right).

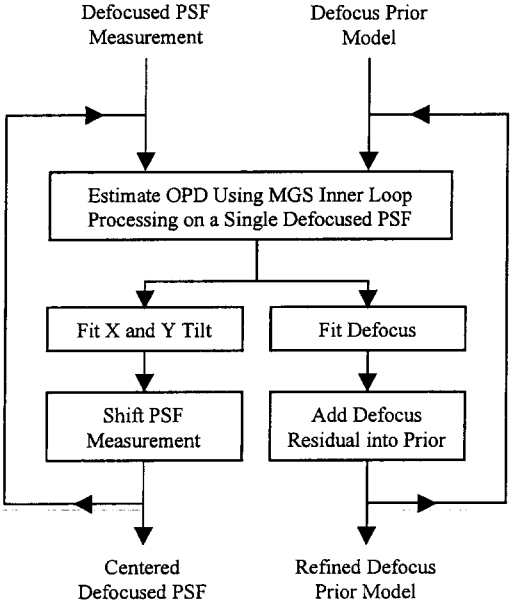

Figure 8: Schematic of preprocessing method for mitigation of centering and defocus prior errors using the MGS algorithm.

5. WFS PERFORMANCE IN THE PRESENCE OF SIMULTANEOUS ERROR SOURCES

Although the error sources we have examined in this paper are fundamentally independent of each other, it may not be the case that their combined impact upon the WFS algorithm will maintain this independence. The concern is that the joint effect of these error sources may yield unacceptable levels of WFS error. In this section, we examine the WFS algorithm performance in the simultaneous presence of noise and modeling errors.

Looking back over the range of error sources, we selected levels for the noise and modeling errors that are acceptable on an independent basis. Table 1 lists the choices of noise and modeling errors that we simultaneously introduce into our simulations.

Table 1:Noise and modeling errors for the joint sensitivity study

Error Source	Comment / Error Level
Poisson Noise	$2x10^{10}$ total photons / defocused PSF
Read Noise	0.5 electrons rms (after combining frames in a defocus level)
Pupil Amplitude Knowledge	0.2 percent rms
Incoherent Blurring	0.5 Nyquist pixels rms
Optical Passbands	0.01 waves
Pixel Area	Binned down by a factor of 2 after over-sampling
Centering Errors	0.1 Nyquist pixels rms / frame
Defocus Model	0.02 waves p-v

As in independent error studies, we collected statistics of the WFS performance over a range of aberration and defocus levels. After realizing pairs of symmetrically defocused PSFs, we applied the MGS based preprocessing method as shown in figure 9. Once the PSF measurements were independently centered and their respective prior defocus models were refined, we ran the nominal MGS algorithm with 250 inner iterations. After the inner-loops were completed, we combined the independent estimates together as described by equation (7) to yield the final estimate. Examples of the WFS error as a function of spatial bandwidth for 4 and 8 waves of symmetric defocus are shown in figure 9.

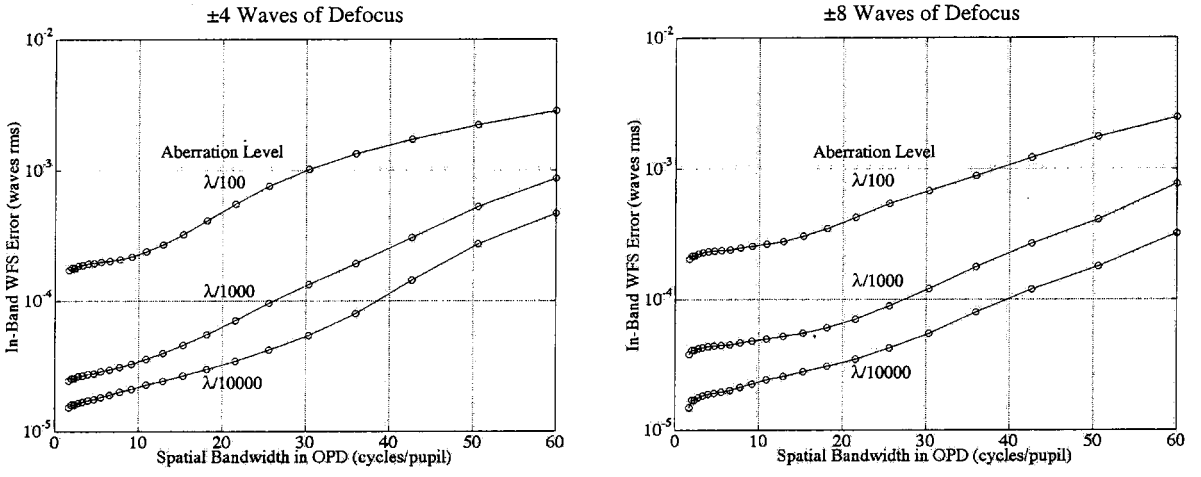

Figure 9: WFS error induced by simultaneous noise and modeling errors for ±4 waves (left) and ±8 waves (right) of focus diversity.

In each plot, the WFS error is shown for three levels of aberration in the system. As the spatial bandwidth of interest increases, we accumulate more WFS error. As we move from ±4 waves to ±8 waves of focus diversity, there are modest improvements in the extent of the WFS spatial bandwidth for a fixed level of admissible WFS error. The key result shown in this figure is really that the WFS error decreases with diminishing WFE. Thus as we correct the system aberrations with a DM, the WFS error over fixed controllable spatial passband decreases.

We obtained the results shown in figure 9 by requiring perfectly symmetric focus diversity in our PSF pairs. As we have shown in this paper, this symmetry plays a central role in the cancellation of fixed model mismatches. As it is not practical to require absolute symmetry in the focus diversity, we examined the increase in WFS error caused by a small asymmetry in the focus levels.

In figure 10, we show the WFS performance of the ±8 waves of defocus case in the presence of the noise and modeling errors. With increasing levels of asymmetry in the defocus levels there is a clear reduction in the WFS accuracy. Depending on the required spatial bandwidth of the OPD, a pair of defocused PSF measurements must be symmetric

about focus to within a few hundredths of a wave. Of coarse after the asymmetry is estimated, an appropriate level of defocus may be induced to reinstate a high level of symmetry in the next set of defocused PSF measurements.

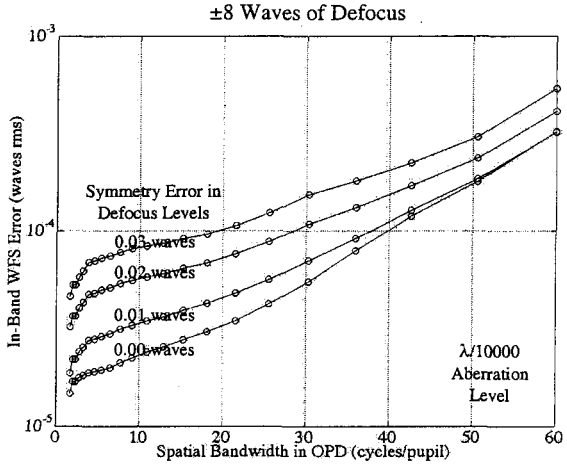

Figure 10: WFS performance of ±8 waves focus diversity in the presence of increasing defocus asymmetry.

5. CLOSING REMARKS

To directly image planets, the Eclipse telescope requires an extremely accurate wave front sensing and control system. To this end, we established key data requirements and processing strategies that enable the MGS WFS algorithm to provide sub-Angstrom level accuracies in its estimates of the exit-pupil WFE. Using sets of Monte Carlo simulations we developed empirical model that relates the MGS WFS error to total integrated flux in a PSF measurement. Remarkably, this relationship appears to be in good agreement with the variance WFS error in the RLP approach. This agreement suggests that there is equivalence of sensing at the occulting plane and the RLP in the absence of other error sources.

In addition to Poisson noise we examined many forms of model mismatch. For fixed modeling errors, we demonstrated the tremendous error reduction brought forth by processing symmetrically defocused PSF pairs. For non-stationary modeling errors we developed a preprocessing method that adapts the data and optical model by using the relevant optical signals that are recovered in the single frame OPD estimates. Finally, we examined the joint error sensitivity of the assortment of noise and modeling errors and demonstrated that $\lambda/10000$ is achievable over a substantial spatial passband for reasonably symmetric pairs of defocused PSF measurement.

As was observed earlier, the great performance benefits that come about with processing symmetrically defocused PSF pairs are also found curvature sensors. We plan to explore the relationship of the MGS algorithm with symmetric focus diversity to the methods employed by curvature sensing. As we continue our efforts to understand the fundamental limits of accurate WFS, we will examine the role of the aberration signal contrast in the defocused PSF measurements, [14], has in our WFS accuracy. In general, we hope to develop a more theoretical basis for understanding the error sensitivities that were present here.

In addition to the planned theoretical developments, we are currently implementing and testing the MGS algorithm with our preprocessing method on the Eclipse high-contrast test-bed, [15]. As this optical system is built up, we will have the ability to experimentally test and validate the accuracy of this and other WFS approaches.

ACKNOWLEDGEMENTS

The research described in this paper was carried out at the Jet Propulsion Laboratory, California Institute of Technology, under a contract with the National Aeronautics and Space Administration.

REFERENCES

1. J. Trauger, "Eclipse mission: a direct survey of nearby planetary systems," Proc. SPIE vol. 4854 (Waikoloa 2002).
2. J. Trauger, et al, "Performance of a precision high-density deformable mirror for extremely high contrast imaging astronomy from space," Proc. SPIE, vol. 4854 (Waikoloa 2002).
3. F. Malbet, J. W. Yu and M. Shao, "High Dynamic-Range Imaging Using a Deformable Mirror for Space Coronography," PASP, v. 107, pp. 386-398, 1995.
4. S. Shaklan, D. Moody and J. J. Green, "Residual Wave Front Phase Estimation in the Reimaged Lyot Plane for the Eclipse Coronagraphic Telescope," Proc. SPIE, vol. 4860 (Waikoloa 2002).
5. J. J. Green, D. C. Redding, Y. Beregovski, Andrew E. Lowman and Catherine M. Ohara, "Interferometric validation of image based wavefront sensing for NGST," Proc. SPIE vol. 4850 (Waikoloa 2002).
6. S. A. Basinger, D. C. Redding, A. E. Lowman, L. A. Burns, K. Liu and D. Cohen, "Performance of wave front sensing and control algorithms on a segmented telescope testbed," Proc. SPIE, *UV, Optical and IR Space Telescopes and Instruments*, V 4013, pp. 749-756 (2000).
7. J. D. Gaskill, *Linear Systems, Fourier Transforms, and Optics*, John Wiley & Sons, New York, 1978.
8. R. W. Gerchberg and W. O. Saxton, "A Practical Algorithm for the Determination of Phase from Image and Diffraction Plane Pictures," *Optik*, vol. 34(2), pp. 237-246. 1972.
9. D. L. Misell, "A method for the solution of the phase problem in electron microscopy," J. Phys. D: Appl. Phys., vol. 6, 1973.
10. B. R. Frieden, *Probability, Statistical Optics, and Data Testing*, Springer-Verlag, Berlin, 1991.
11. D. J. Schroeder, *Astronomical Optics*, Academic Press, San Diego, 2000.
12. F. Roddier, ed., *Adaptive Optics in Astronomy,* Cambridge University Press, New York, 1999.
13. R. J. Noll, "Zernike polynomials and atmospheric turbulence," J. Opt. Soc. Am., vol. 66(3), pp. 207-211, 1976.
14. B. Dean, "Diversity Selection for Phase-Diverse-Phase-Retrieval", J. Opt. Soc. Am. A., In Preparation, 2002.
15. J. Trauger, et al, "Eclipse high-contrast imaging test bed," Proc. SPIE, vol. 4854 (Waikoloa 2002).